



A Complex Dust Morphology in the High-luminosity AGN Mrk 876

Hermine Landt¹, Jake A. J. Mitchell¹, Martin J. Ward¹, Paul Mercatoris², Jörg-Uwe Pott², Keith Horne³,
Juan V. Hernández Santisteban³, Daksh Malhotra^{3,4}, Edward M. Cackett⁵, Michael R. Goad⁶,
Encarni Romero Colmenero^{7,8}, and Hartmut Winkler⁹

¹ Centre for Extragalactic Astronomy, Department of Physics, Durham University, South Road, Durham, DH1 3LE, UK; hermine.landt@durham.ac.uk

² Max Planck Institut für Astronomie, Königstuhl 17, D-69117 Heidelberg, Germany

³ SUPA Physics and Astronomy, University of St. Andrews, Fife, KY16 9SS, UK

⁴ Department of Physics, University of Alberta, 4-181 CCIS, Edmonton, AB T6G 2E1, Canada

⁵ Wayne State University, Department of Physics & Astronomy, 666 W Hancock St, Detroit, MI 48201, USA

⁶ Department of Physics and Astronomy, University of Leicester, University Road, Leicester, LE1 7RH, UK

⁷ Southern African Large Telescope (SALT), P.O. Box 9, Observatory 7935, Cape Town, South Africa

⁸ The South African Astronomical Observatory (SAAO), P.O. Box 9, Observatory 7935, Cape Town, South Africa

⁹ Department of Physics, University of Johannesburg, P.O. Box 524, 2006 Auckland Park, Johannesburg, South Africa

Received 2022 December 12; revised 2023 February 1; accepted 2023 February 2; published 2023 March 7

Abstract

Recent models for the inner structures of active galactic nuclei (AGNs) advocate the presence of a radiatively accelerated dusty outflow launched from the outer regions of the accretion disk. Here, we present the first near-IR variable (rms) spectrum for the high-luminosity nearby AGN Mrk 876. We find that it tracks the accretion disk spectrum out to longer wavelengths than the mean spectrum, due to a reduced dust emission. The implied outer accretion disk radius is consistent with the IR results predicted by a contemporaneous optical accretion disk reverberation mapping campaign, and much larger than the self-gravity radius. The reduced flux variability of the hot dust could either be due to the presence of a secondary constant dust component in the mean spectrum or be introduced by the destructive superposition of the dust and accretion disk variability signals, or be some combination of the two. Assuming thermal equilibrium for optically thin dust, we derive the luminosity-based dust radii for different grain properties, using our measurement of the temperature. We find that in all the cases considered, the values are significantly larger than the dust response time measured by IR photometric monitoring campaigns, with the least discrepancy present relative to the result for a wavelength-independent dust emissivity law, i.e., a blackbody, which is appropriate for large grain sizes. This result can be well explained by assuming a flared disk-like structure for the hot dust.

Unified Astronomy Thesaurus concepts: Active galactic nuclei (16); Quasars (1319); Dust continuum emission (412); Dust physics (2229); Near infrared astronomy (1093)

1. Introduction

Most active galactic nuclei (AGNs) display prominent IR emission in their spectral energy distributions (SEDs), which can be attributed to thermal dust radiation. This central dusty structure is commonly assumed to be optically thick and to have a toroidal geometry that is aligned with the plane of the accretion disk. The latter requirement was mainly derived from the need for an equatorial obscurer in AGNs, in order to account for the observations of broad emission lines in the polarized scattered light of many type 2 AGNs and the relative numbers of type 1 and type 2 AGNs in complete samples (see the reviews by Lawrence 1987; Antonucci 1993; Netzer 2015; Lyu & Rieke 2022a). A warped dusty disk could be a viable alternative to the dusty torus, as first proposed by Phinney (1989). The extended dusty torus emits over a large range of IR wavelengths, with the hottest dust observed in the near-IR believed to be located closest to the central supermassive black hole, whereas warm dust (of a few 100 K) is observed in the mid-IR and expected to be located on average farther out (Weedman et al. 2005; Buchanan et al. 2006; Landt et al. 2010; Lyu & Rieke 2018; Brown et al. 2019). Often, cold dust (of a

few 10 K) emitting at far-IR wavelengths is also observed in AGNs, although this component is most likely heated by young stars in the host galaxy, rather than by the UV and optical emission of the central accretion disk (Kirkpatrick et al. 2015).

AGNs are ideal laboratories for investigating the chemical composition and grain properties of astrophysical dust. Their UV/optical luminosities are usually high enough to heat the circumnuclear dust to sublimation temperatures. If these highest values can be observed, they can in principle constrain the chemistry, since different species condense out of the gas phase in different environmental conditions. Dust temperatures have been measured with simultaneous photometry at several near-IR wavelengths in a handful of sources (Clavel et al. 1989; Glass 2004; Schnülle et al. 2013, 2015), but this process has only come of age with the availability of efficient near-IR cross-dispersed spectrographs. Landt et al. (2011b, 2014) have derived dust temperatures from such spectroscopy for the largest sample of type 1 AGNs so far (~30 sources). Their measurements yielded a very narrow temperature distribution, with an average value of $T \sim 1400$ K. This result indicated that if the hot dust is indeed at sublimation, it is composed of only silicate dust grains, so the environment in which the dust formed must have been oxygen-rich. However, if carbon is present, then the dust is not heated to close to sublimation, since carbonaceous dust, e.g., graphite, can survive up to $T \sim 2000$ K (Salpeter 1977).



Original content from this work may be used under the terms of the [Creative Commons Attribution 4.0 licence](https://creativecommons.org/licenses/by/4.0/). Any further distribution of this work must maintain attribution to the author(s) and the title of the work, journal citation and DOI.

The range in temperatures within the dusty torus roughly translates to a range in radius, allowing mainly the mid-IR emitting dust to be spatially resolved with current instruments. High-angular resolution mid-IR imaging (Ramos Almeida et al. 2011) and mid-IR interferometry (e.g., Tristram et al. 2009; Burtscher et al. 2013) of a dozen nearby and bright AGNs have delivered useful upper limits on the extent of the dusty torus (of up to a few parsecs). Such spatially resolved observations have also revealed a significant warm dust component perpendicular to the plane of the accretion disk, referred to as “polar dust” (Hönig et al. 2013; Tristram et al. 2014; Gámez Rosas et al. 2022; Isbell et al. 2022; Lyu & Rieke 2022b), which was also evident from SED studies (Landt et al. 2010; Isbell et al. 2021). GRAVITY, the near-IR interferometric instrument at the Very Large Telescope, has started to resolve the innermost and hottest part of the central dusty structure in some nearby luminous sources (Gravity Collaboration et al. 2020), and further progress is expected from an upgrade in sensitivity to GRAVITY+. But for most AGNs, knowledge about the inner dust radius is most efficiently obtained through dust reverberation, which is a technique that measures the time response of the dust to the variable irradiating accretion disk flux. For ~ 60 AGNs, the hot dust radii have been determined by photometric campaigns, often coordinated at optical and near-IR wavelengths (e.g., Clavel et al. 1989; Nelson 1996; Oknyanskij & Horne 2001; Glass 2004; Suganuma et al. 2006; Schnülle et al. 2013, 2015; Koshida et al. 2014; Vazquez et al. 2015; Lyu et al. 2019; Minezaki et al. 2019). In general, the observed dust response times follow a luminosity–radius relationship, with a slope similar to that for the broad emission line region (BLR), indicating a roughly constant hot dust flux and thus a narrow hot dust temperature distribution. However, the dust radii measured via reverberation are often smaller (by factors of a few) than the dust radii measured by interferometry or estimated from SEDs, assuming thermal equilibrium (Kishimoto et al. 2007; Nenkova et al. 2008; Landt et al. 2014). A possible interpretation of this finding is that the dust has a bowl-shaped geometry that is caused by the anisotropy of the accretion disk emission irradiating it (Kawaguchi & Mori 2010, 2011). In such a geometry, the hot dust that is located in the plane of the accretion disk is placed farther in than the bulk of the dust, and so it is expected to dominate the reverberation signal.

Developments in technology and flexible scheduling have now made spectroscopic near-IR monitoring campaigns feasible. Landt et al. (2019) presented the first such program. Using a near-IR cross-dispersed spectrograph with a relatively wide wavelength coverage that extends partially into the optical, they showed that such a campaign allowed the following for low-redshift AGNs: (i) the monitoring of a large portion of the hot dust SED, which readily gives the dust temperature and its evolution; (ii) the separation of the accretion disk emission from that of the hot dust, which is a considerable source of error in photometric campaigns; (iii) the simultaneous determination of luminosity-based and response-weighted dust radii; (iv) the construction of the variable (rms) near-IR spectrum; and (v) the ability to study the variability of the emission lines formed in the BLR and the coronal line region. Their study of the hot dust in NGC 5548 found that a single component dominated both the mean emission and variations, with the dust response time and the luminosity-

based dust radius being consistent with each other only if a blackbody emissivity was assumed. This result constrained the dust grain size to a few microns. The temperature and its variability indicated carbonaceous dust well below the sublimation threshold, undergoing a heating and cooling process in response to the variable UV/optical accretion disk flux irradiating it. Most importantly, the dust reverberation signal showed tentative evidence for a second hot dust component, most likely associated with the accretion disk. The existence of such dust is a prerequisite for the recent models of AGN structure proposed by Czerny et al. (2017) and Baskin & Laor (2018), which explain both the BLR and the dusty torus as part of the same outflow, launched from the outer regions of the accretion disk by the radiation pressure on dust—preferentially on carbonaceous dust, since it has a higher opacity than silicate dust.

Here, we present the results from a near-IR spectroscopic monitoring campaign on Mrk 876 that was conducted between 2016 May and 2017 July. A contemporaneous optical photometric monitoring campaign in several bands was conducted between 2016 March and 2019 May and Miller et al. (2023) have recently presented the accretion disk reverberation results from these data. The structure of our paper is as follows. In Section 2, we discuss the science target, and we give the details of the near-IR observations and data reduction in Section 3. In Sections 4 and 5, we derive the luminosity-based dust radius and the variable (rms) spectrum, respectively. We discuss our main results in Section 6, where we seek a relation between the central dust structures observed in AGNs and the protoplanetary disks around young stars. Finally, in Section 7, we present a short summary and our conclusions.

2. The Science Target

Mrk 876 (PG 1613+658) is one of the intrinsically most luminous AGNs in the nearby universe. At a redshift of $z = 0.129$, it has an average V -band luminosity of $\sim 5 \times 10^{44}$ erg s $^{-1}$ (Bentz et al. 2013). This places it at the undersampled top end of the relationship between the hot dust radius and the optical continuum luminosity, as presented by Koshida et al. (2014) and Minezaki et al. (2019). The latter study performed for Mrk 876 a coordinated optical and near-IR photometric campaign during the years 2003–2007, measuring dust response times of $\tau = 320 \pm 34$, 327_{-36}^{+42} , and 327_{-35}^{+41} lt-days, assuming different values for the accretion disk power-law spectral slope when decomposing the flux in the K band. A similar dust response time was obtained also by Lyu et al. (2019), who combined optical photometric light curves from ground-based transient surveys with WISE monitoring data for the years 2010–2018. They estimated dust response times of $\tau = 372 \pm 63$ and 390 ± 37 lt-days for the W1 and W2 bands, respectively. Finally, Afanasiev et al. (2019) performed spectropolarimetric observations of Mrk 876 in 2015 and constrained the distance to the equatorial scattering region to 254 ± 39 lt-days, which they assumed was the inner radius of the dusty torus.

Mrk 876 has a relatively high black hole mass, which has been well determined by optical reverberation campaigns, of $M_{\text{BH}} = (2.2 \pm 1.0) \times 10^8 M_{\odot}$ (Peterson et al. 2004; Bentz & Katz 2015), transformed from the measured virial product using a scaling factor of $f = 4.3$ (Grier et al. 2013). For this black hole mass, the corresponding gravitational radius is

Table 1
Gemini Journal of Observations

Observation Date (1)	Exposure (s) (2)	Airmass (3)	Aperture (arcsec ²) (4)	PA (°) (5)	Continuum S/N			Telluric Star Airmass (9)	Correction Factor	
					<i>J</i> (6)	<i>H</i> (7)	<i>K</i> (8)		PREPSPEC (10)	MAPSPEC (11)
2016 May 25	8 × 120	1.553	0.675 × 1.25	143	77	112	180	1.591	1.01 ± 0.03	1.12
2016 Jun 16	8 × 120	1.438	0.675 × 1.11	165	104	217	105	1.392	0.71 ± 0.04	0.83
2016 Jul 15	8 × 120	1.490	0.675 × 0.95	146	124	154	201	1.401	1.11 ^{+0.14} _{-0.12}	1.12
2016 Aug 4	8 × 120	1.455	0.675 × 1.09	158	87	115	212	1.422	0.99 ^{+0.10} _{-0.09}	1.18
2017 Feb 24	8 × 120	1.485	0.675 × 1.28	190	105	245	145	1.372	1.23 ± 0.05	1.31
2017 Apr 4	8 × 120	1.755	0.675 × 1.27	174	105	139	187	1.706	0.97 ± 0.05	1.08
2017 Apr 16	8 × 120	1.481	0.675 × 1.08	201	118	162	160	1.416	1.15 ± 0.03	1.21
2017 May 4	6 × 120	1.439	0.675 × 1.26	187	109	93	165	1.362	0.88 ^{+0.05} _{-0.04}	0.87
2017 Jun 3	8 × 120	1.443	0.675 × 1.18	174	96	102	104	1.414	0.99 ^{+0.08} _{-0.07}	1.07
2017 Jul 5	8 × 120	1.489	0.675 × 1.40	174	72	110	194	1.423	1.43 ± 0.04	1.63

Note. Column (1): universal time date of observation. Column (2): exposure time. Column (3): mean airmass. Column (4): extraction aperture. Column (5): slit position angle, where PA = 0° corresponds to north–south orientation and is defined as north through east. Columns (6)–(8): the S/N in the continuum over ~100 Å, measured at the central wavelengths of the *J*, *H*, and *K* bands, respectively. Column (9): the mean airmass for the telluric standard star. Columns (10)–(11): the multiplicative photometric correction factor, determined using the narrow emission line [S III] λ 9531 within the PREPSPEC and MAPSPEC routines, respectively.

$r_g = 3.2 \times 10^{13}$ cm = 0.013 lt-days, where $r_g = GM_{\text{BH}}/c^2$, with G being the gravitational constant and c the speed of light. The corresponding Eddington luminosity is $L_{\text{edd}} = 2.7 \times 10^{46}$ erg s⁻¹. The optical emission line spectrum of Mrk 876 is of the inflected type—i.e., the broad line profiles have clearly discernible broad- and narrow-line components. The hydrogen BLR radius has recently been measured by an optical spectroscopic reverberation mapping campaign, during the years 2016–2021, as being in the range of ~40–50 lt-days, based on the response time of the optical Balmer line Hβ (Bao et al. 2022).

Mrk 876 (J2000 sky coordinates R.A. 16^h13^m57^s.2, decl. +65°43′10″) is only observable from the northern hemisphere. Its low redshift and high intrinsic luminosity make it sufficiently bright in the near-IR (2MASS *J* = 13.2 mag, *K_s* = 11.4 mag; Skrutskie et al. 2006), so that a high-quality spectrum can be achieved in a relatively short exposure time. We adopt the cosmological parameters $H_0 = 70$ km s⁻¹ Mpc⁻¹, $\Omega_M = 0.3$, and $\Omega_\Lambda = 0.7$, which give a luminosity distance to Mrk 876 of 605.2 Mpc and an angular scale at the source of 2302 pc per arcsec.

3. The Observations

3.1. The Near-IR Spectroscopy

We observed Mrk 876 between 2016 May and 2017 July at the Gemini North 8 m Observatory on Maunakea, Hawaii, in queue mode (Program IDs: GN-2016A-FT-27 and GN-2017A-Q-41), using the Gemini Near-Infrared Spectrograph (GNIRS; Elias et al. 2006). We obtained roughly one spectrum per month, except for a gap period of about five months (from September to January), when Mrk 876 is not observable, resulting in a total of 10 near-IR spectra. Table 1 lists the journal of observations. The sky was clear and the seeing was very good (~0″4–0″6) for all nights, except 2016 June 16, 2017 February 24, and 2017 July 5, when some clouds were present and the seeing was variable. We used the cross-dispersed mode with the short camera at the lowest spectral resolution (31.71 mm⁻¹ grating), thus covering the entire wavelength range of 0.85–2.5 μm, without interorder contamination. We chose a slit of 0″675 × 7″, which we oriented at

the parallactic angle. This setup gives an average spectral resolution of FWHM ~ 400 km s⁻¹. The on-source exposure time of 8 × 120 s ensured that we obtained spectra with high signal-to-noise ratios (S/Ns), in order to reliably measure the emission line profiles. Since the source is not extended in the near-IR, we nodded along the slit in the usual ABBA pattern. The observations were taken on average at an airmass of sec *z* ~ 1.5, which is close to the minimum value achievable for this source from Hawaii.

After or before the science target, we observed the nearby (in position and airmass) F0 V star HIP 79087 (HD 145710), which has accurate near-IR magnitudes. We used this standard star to correct our science spectrum for telluric absorption and flux calibration. For the flux calibration, we assumed that its continuum emission could be approximated by a blackbody with an effective temperature of $T_{\text{eff}} = 6769$ K (Soubiran et al. 2016). Flats and arcs were taken after the science target.

We reduced the data using the Gemini/IRAF package, with GNIRS-specific tools (Cooke & Rodgers 2005). The data reduction steps included the preparation of calibration and science frames, the processing and extraction of spectra from the science frames, the wavelength calibration of the spectra, the telluric correction and flux calibration of the spectra, and the merging of the different orders into a single continuous spectrum. The spectral extraction width was adjusted interactively for the telluric standard star and the science source, to include all the flux in the spectral trace. A local averaged background flux was fitted and subtracted from the total source flux. The final spectrum was corrected for Galactic extinction using the IRAF task *onedspec.deredden*, with an input value of $A_V = 0.005$, which we derived from the Galactic hydrogen column densities published by Dickey & Lockman (1990). In Figure 1, we show the spectrum from 2016 May 25 as a representative example.

3.2. The Complementary Photometry

Mrk 876 was monitored with the 1 m robotic telescope network of the Las Cumbres Observatory (LCOGT; Brown et al. 2013) as part of the 2014 AGN Key Project, on an almost daily basis, in four bands (*g*, *r*, *i*, and *z_s*), between 2016 February 12 and 2020 October 10, but with the *z_s* band

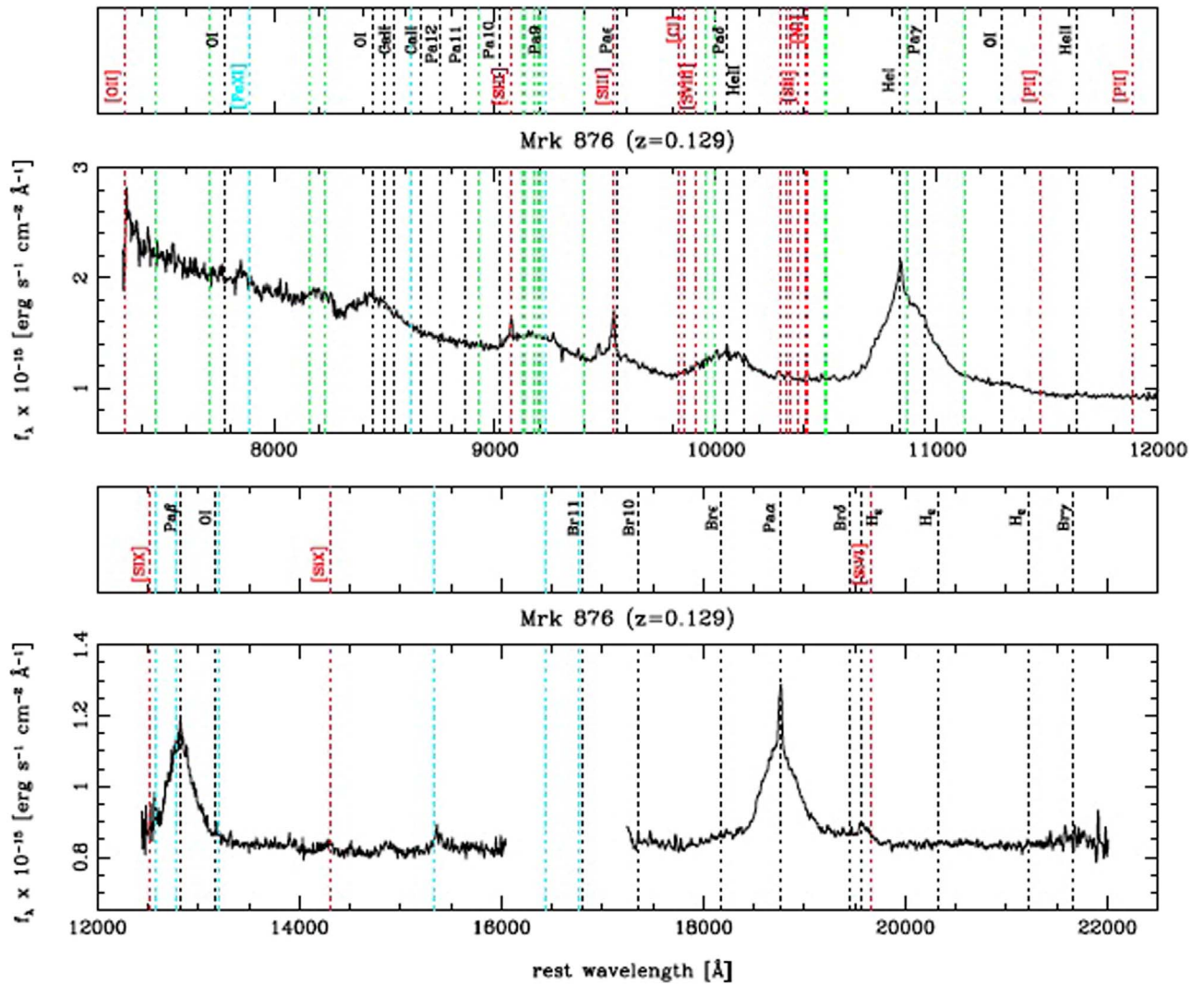


Figure 1. Gemini GNIRS near-IR spectrum from 2016 May 25, shown as observed flux vs. rest-frame wavelength. Emission lines that are listed in Table 4 of Landt et al. (2008) are marked by the dotted lines and labeled—black: permitted transitions; green: permitted Fe II multiplets (not labeled); red: forbidden transitions; and cyan: forbidden transitions of iron (those of [Fe II] not labeled).

switched off in the period from 2017 April 4 to 2018 June 17. We make use here of the light curves in the g and z_s filters, which have wavelength widths of 1500 \AA and 1040 \AA around their central wavelengths of 4770 \AA and 8700 \AA , respectively. The LCOGT Sinistro cameras have a field of view of $26'.5 \times 26'.5$ and a plate scale of $0''.389$ per pixel.

The frames were first processed by LCOGT's BANZAI pipeline (McCully et al. 2018) in the usual way (bias and dark subtraction, flat-fielding correction, and cosmic-ray rejection), and they were subsequently analyzed with the custom-made pipeline described in detail by Hernández Santisteban et al. (2020). In short, after performing aperture photometry with a diameter of $7''$ and subtracting a background model, stable light curves were produced by constructing a curve of growth, using the standard stars on each individual frame and measuring the correction factors required to bring all the different light curves to a common flux level. A color correction and a correction for atmospheric extinction were applied before the photometric calibration. Finally, an image zeropoint calibration was performed at each epoch, based on comparison stars in the field. In Figure 2 (top two panels), we

display the g and z_s light curves, with the latter overlapping in wavelength with the GNIRS near-IR spectrum.

3.3. The Absolute Spectral Flux Scale

In order to derive light curves, construct meaningful mean and variable (rms) spectra, and estimate luminosities, we must achieve an accurate absolute flux calibration of the spectra. Similar to the approach that has been chosen by optical spectroscopic reverberation campaigns to achieve this, we base our absolute spectral flux scale on a strong narrow emission line from a forbidden transition. Such emission lines are expected to remain constant during the campaign, since they are produced in gas that is located at distances of parsec to kiloparsec scales from the ionizing source and that has a number density that is low enough for recombination time-scales to be large. We have chosen the [S III] $\lambda 9531$ line, since it is the strongest narrow forbidden emission line in the near-IR. It is blended with the Pa ϵ broad emission line, but it can easily be separated from it, since this hydrogen line is usually weak. Imaging studies of the [S III] $\lambda 9531$ line have been performed on a few nearby AGNs, using near-IR integral-field

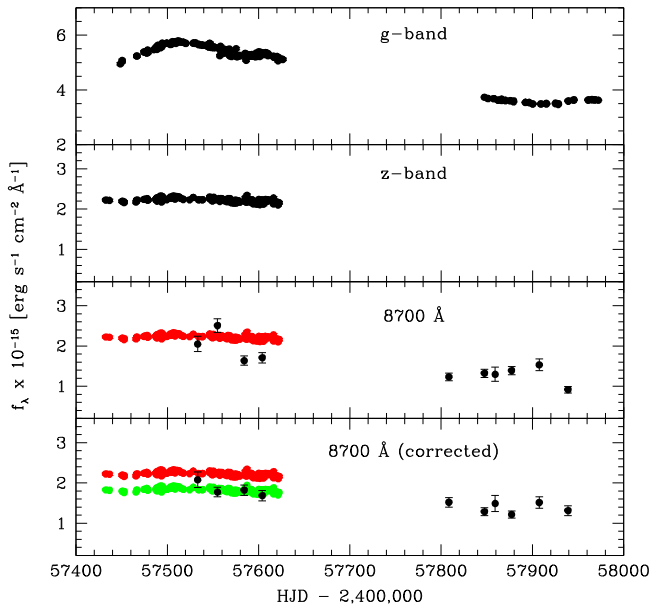


Figure 2. Top two panels: LCOGT g - and z_s -band light curves from 2016 February to 2017 July. Bottom two panels: Gemini GNIRS near-IR spectral light curve around the observed wavelength of 8700 \AA (filled black circles), both original and corrected, using PREPSPEC photometric correction factors, based on the [S III] $\lambda 9531$ line, vs. the z_s -band light curve (filled red circles). The z_s -band light curve, corrected for a constant host galaxy contribution to match the near-IR spectral fluxes, is also shown (filled green circles).

spectrographs, and the gas forming this line has been found to be extended on moderate scales of up to a few 100 pc (e.g., Storchi-Bergmann et al. 2009; Fischer et al. 2015, 2017). Our slit size of $0''.675$, centered on the nucleus, corresponds to a radial extent of ~ 800 pc, which is sufficiently large to ensure that all the [S III] line flux is enclosed in the spectral extraction aperture.

We have used two routines to determine the photometric correction factors for our observations: the PREPSPEC routine developed by Keith Horne (last described in Horne et al. 2021) and the MAPSPEC routine of Fausnaugh (2017). In short, PREPSPEC models both the emission lines and the total continuum, and subsequently matches the profiles of selected narrow emission lines in the spectra, in order to derive the time-dependent scaling factor. It assumes that the majority of the spectra are photometric, and so holds the median photometric correction factor at 1. The MAPSPEC routine constructs a reference spectrum by averaging the highest-quality spectra, e.g., those spectra that have the highest S/Ns and/or were observed under the best weather conditions. The profile of the chosen narrow emission line is then matched between the reference spectrum and the individual spectra. The spectral scaling factors resulting from the two routines are listed in Table 1. With the exception of the last observational epoch, the results from PREPSPEC and MAPSPEC are consistent within the errors, but there is a trend for the former correction factors to be lower than the latter. In the following, we use the PREPSPEC correction factors, which span a range of $\sim 1\%$ – 40% , with an average value of $\sim 10\%$. In Figure 2 (bottom two panels), we show the GNIRS near-IR spectral continuum flux in the observed wavelength range of the LCOGT z_s -band filter, centered at 8700 \AA , both original and corrected. If we subtract from the z_s -band light curve a constant host galaxy flux contribution of $\sim 20\%$ of the total flux, it matches very well with all four of the corrected near-IR spectral flux

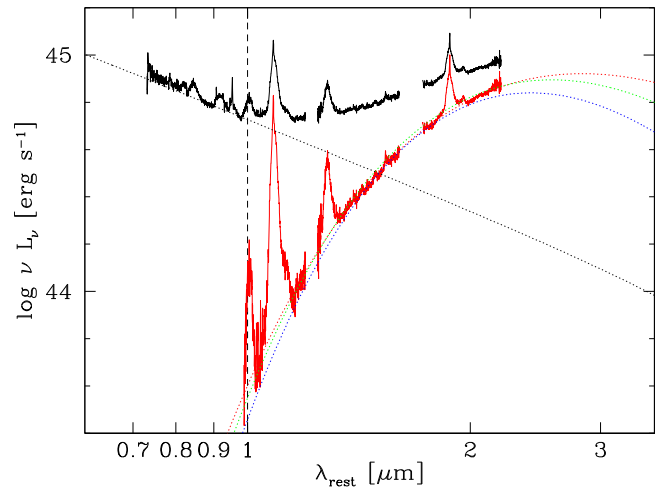


Figure 3. Gemini GNIRS near-IR spectrum from 2016 May 25, shown as luminosity vs. rest-frame wavelength (black spectrum). We decompose the continuum into two components: an accretion disk spectrum that approximates the wavelength range $\lesssim 1 \mu\text{m}$ (dotted black curve) and still dominates at $1 \mu\text{m}$ (vertical dashed line) and a hot dust emission (red spectrum). We fit the hot dust continuum with a blackbody spectrum (dotted red curve) and modified blackbody spectra for carbon and silicate dust (dotted green and blue curves, respectively), with the resulting best-fit temperatures as listed in Table 2.

measurements in the time of overlap. For the later epochs, the g -band light curve shows a downward trend in flux, which is also reproduced.

4. The Luminosity-based Dust Radius

In order to be able to derive luminosity-based dust radii, we need to measure the dust temperature and estimate the UV/optical accretion disk luminosity that heats the dust. In Mrk 876, the relatively large wavelength range of the cross-dispersed near-IR spectra simultaneously covers about half the hot dust SED and a considerable part of the accretion disk spectrum, which is expected to dominate the total continuum flux up to $\sim 1 \mu\text{m}$ (Landt et al. 2011a, 2011b). Therefore, we decompose the spectral continuum into two components, following the approach described in Landt et al. (2019) and exemplified in Figure 3. We note that since we use a relatively small spectral aperture, the contribution of the host galaxy light to the total observed continuum flux is negligible in this luminous AGN. In short, we first approximate the rest-frame wavelength range of $\lesssim 1 \mu\text{m}$ with the spectrum of a standard accretion disk, which we subsequently subtract from the total spectrum. For the calculation of the accretion disk spectrum, we adopt the black hole mass given in Section 2, while the accretion rate is obtained directly from the scaling to the data. Furthermore, we assume that the disk is relatively large and extends out to $r_{\text{out}} = 10^4 r_g$. We then fit the resultant hot dust spectrum at wavelengths $> 1 \mu\text{m}$ with a blackbody, representing emission from large dust grains, and also with two blackbodies modified by a power law of the form $Q_\lambda(a) \propto \lambda^\beta$, approximating with $\beta = -1$ and $\beta = -2$ the emissivity of the submicron silicate and carbon dust grains, respectively (Landt et al. 2019; see their Figure 8). We note in Figure 3 the excellent agreement between the data and the standard accretion disk spectrum that we assume here, a result that is generally found for AGNs with negligible contributions from host galaxy light (e.g., Koratkar & Blaes 1999; Landt et al. 2011b). Table 2 lists the physical parameters derived from the

Table 2
Physical Parameters for the Calculation of Luminosity-based Dust Radii

Observation Date	Accretion Disk	Blackbody			Silicate Dust			Carbon Dust		
		$(\beta = 0, \langle Q^{\text{em}} \rangle = 1)$			$(\beta = -1, \langle Q^{\text{em}} \rangle = 0.0210)$			$(\beta = -2, \langle Q^{\text{em}} \rangle = 0.0875)$		
(1)	(2)	T_d (K)	$\log L_d$ (erg s^{-1})	$R_{d,\text{lum}}$ (lt-day)	T_d (K)	L_d (erg s^{-1})	$R_{d,\text{lum}}$ (lt-day)	T (K)	L_d (erg s^{-1})	$R_{d,\text{lum}}$ (lt-day)
2016 May 25	46.22	1297 ± 13	45.55	554	1126 ± 11	44.73	5070	996 ± 8	45.28	3175
2016 Jun 16	46.19	1305 ± 9	45.71	681	1133 ± 7	44.84	6232	1001 ± 5	45.70	3912
2016 Jul 15	46.18	1325 ± 11	45.51	468	1148 ± 9	44.75	4298	1013 ± 7	45.59	2704
2016 Aug 4	46.14	1311 ± 9	45.54	494	1136 ± 7	44.73	4543	1002 ± 6	45.67	2861
2017 Feb 24	46.12	1324 ± 10	45.53	408	1149 ± 7	44.76	3737	1015 ± 6	45.17	2346
2017 Apr 4	46.01	1334 ± 10	45.55	421	1158 ± 7	44.78	3852	1023 ± 5	45.63	2418
2017 Apr 16	46.04	1303 ± 8	45.52	402	1136 ± 6	44.72	3651	1007 ± 5	45.19	2276
2017 May 4	46.00	1308 ± 14	45.61	458	1135 ± 11	44.43	4199	1003 ± 8	45.57	2634
2017 Jun 3	46.01	1267 ± 13	45.55	466	1102 ± 10	44.34	4254	975 ± 8	45.53	2662
2017 Jul 5	46.02	1288 ± 12	45.43	342	1120 ± 9	44.68	3124	991 ± 7	45.03	1955

Note. Column (1): universal time date of observation. Column (2): total accretion disk luminosity. Columns (3)–(5): dust temperature, total dust luminosity, and dust radius for a blackbody emissivity. Columns (6)–(8): dust temperature, total dust luminosity, and dust radius for an emissivity law appropriate for silicate dust, with small grain sizes of $a \lesssim 0.1 \mu\text{m}$. Columns (9)–(11): dust temperature, total dust luminosity, and dust radius for an emissivity law appropriate for carbon dust, with small grain sizes of $a \lesssim 0.1 \mu\text{m}$.

spectral decomposition. The resultant average temperatures and errors on the mean are $\langle T \rangle = 1306 \pm 6$, 1134 ± 5 , and 1033 ± 4 K for emissivity laws with $\beta = 0$, -1 , and -2 , respectively.

As in Landt et al. (2019), we then calculate the luminosity-based dust radii, $R_{d,\text{lum}}$, from the best-fit dust temperatures, assuming radiative equilibrium between the luminosity of the irradiating source and the dust:

$$\frac{L_{\text{uv}}}{4\pi R_{d,\text{lum}}^2} = 4\sigma T^4 \langle Q^{\text{em}} \rangle, \quad (1)$$

where σ is the Stefan–Boltzmann constant and $\langle Q^{\text{em}} \rangle$ is the Planck-averaged value of $Q_\lambda(a)$. We approximate L_{uv} with the accretion disk luminosity at each epoch, as given in Table 2, and we use for the Planck-averaged emission efficiencies in the case of $\beta = -1$ a value of $\langle Q^{\text{em}} \rangle = 0.0210$, which is appropriate for silicates of $T = 1259$ K and $a = 0.1 \mu\text{m}$ (Laor & Draine 1993), and in the case of $\beta = -2$ a value of $\langle Q^{\text{em}} \rangle = 0.0875$, which is appropriate for graphite of $T = 1000$ K and $a = 0.1 \mu\text{m}$ (Draine 2016). The average luminosity-based rest-frame dust radii and the errors on the mean are $\langle R_{d,\text{lum}} \rangle = 469 \pm 30$, 4296 ± 273 , and 2694 ± 172 lt-days in the case of a blackbody, a small-grain silicate, and small-grain carbon dust, respectively.

5. The Variable Near-IR Spectrum

We calculate the mean and variable (rms) near-IR spectra, following Peterson et al. (2004). Figure 4 (top) shows them in comparison. In order to be able to compare the chromatic shapes of the two spectra, we rescale the rms spectrum by a factor of ~ 7 , in order to match the mean optical flux at $0.9 \mu\text{m}$. Assuming a simple flux variability, scaling with the total flux would lead to comparable shapes, but we observe this similarity only in the spectral part that is dominated by the accretion disk. Instead, two spectral continuum features become apparent at wavelengths beyond $\sim 1 \mu\text{m}$. First, the rms spectrum tracks the accretion disk spectrum out to longer wavelengths ($\sim 1.2 \mu\text{m}$) than the mean spectrum ($\sim 1 \mu\text{m}$). This is an important finding, since we do not know the full extent of

the accretion disks, mainly because their IR spectra are overwhelmed by the emission from the hot dust. IR polarimetry can reveal a disk’s near-IR continuum, but only for the brightest AGNs (Kishimoto et al. 2008). In order for the accretion disk spectrum to dominate the emission at $\sim 1 \mu\text{m}$, as observed in the mean spectrum and established by the near-IR radius–luminosity relationship (Landt et al. 2011a), the inferred disk outer radius is $r_{\text{out}} \sim 1500 r_g \sim 20$ lt-days. Observing the optical variable component in the rms spectrum out to $\sim 1.2 \mu\text{m}$ and assuming that it is the accretion disk then implies a value of $r_{\text{out}} \sim 1900 r_g \sim 25$ lt-days. This radius is much larger than the self-gravity radius, i.e., the radius at which accretion disks are generally assumed to become unstable and fragment, which is ~ 12 lt-days (Lobban & King 2022).

Second, the near-IR flux variability relative to the mean continuum flux at $\geq 1 \mu\text{m}$ appears significantly lower than in the visible domain, which is dominated by the accretion disk only. Since the near-IR clearly shows the additional hot dust flux, this behavior could be explained by the systematically reduced flux variability of the hot dust with respect to the accretion disk. This would explain why the accretion disk spectral slope is revealed out to longer wavelengths, a scenario similar to that seen in the mean flux spectrum of the so-called “hot-dust-poor” quasars reported by Hao et al. (2010). A spectral decomposition of the rms and mean spectra, as performed in Section 4, gives a flux ratio reduced by a factor of ~ 3 in the former relative to the latter. The ratio of the rms spectrum to the mean spectrum measures the fractional amplitude of the variations, i.e., the variable flux as a percentage of the mean flux, in dependence of wavelength. If the shape of the variable spectrum is identical to that of the mean spectrum, it means that the fractional variability is independent of wavelength. A reduction of the fractional variability at a given wavelength can be introduced by the presence of a constant component, which would increase the flux in the mean spectrum. Our observed variable near-IR spectrum for Mrk 876 shows a reduced fractional variability for the blackbody component only (Figure 5, bottom panel). We visualize this difference spectrum for wavelengths $\gtrsim 1 \mu\text{m}$, which can be well fitted by a blackbody of temperature

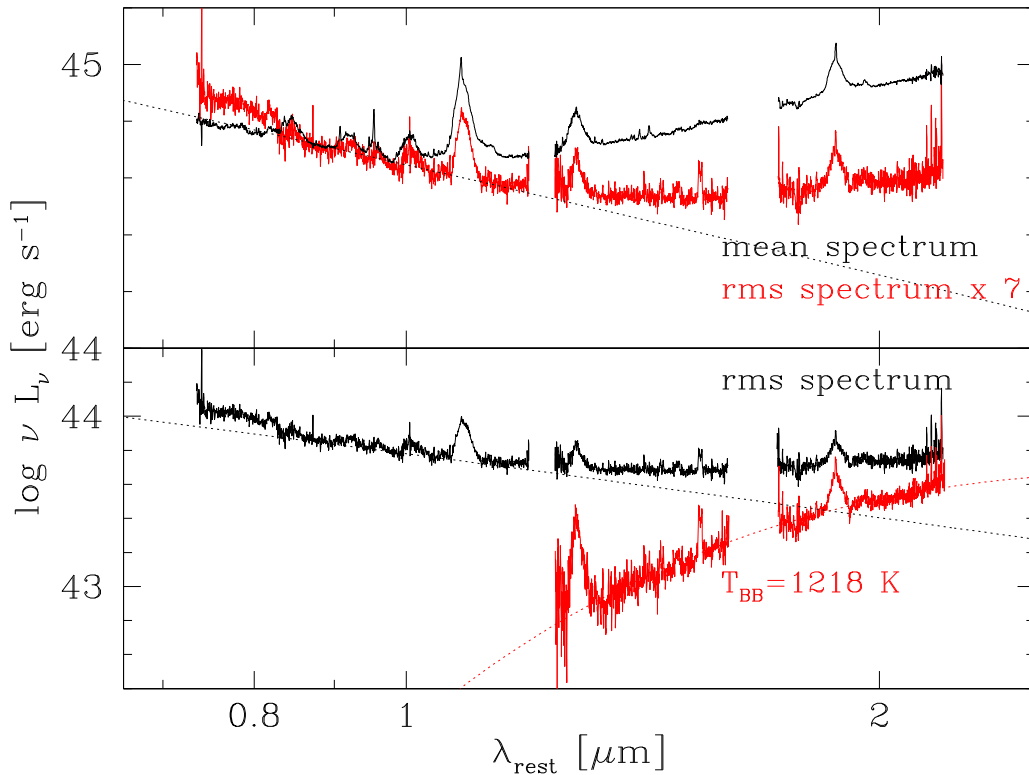


Figure 4. Top: the mean (black) and variable near-IR (red) spectra for our campaign, normalized at rest frame $0.9 \mu\text{m}$. The spectrum of a standard accretion disk (dotted black line) is traced to $\sim 1.2 \mu\text{m}$ in the variable component and only to $\sim 1 \mu\text{m}$ in the mean spectrum. Bottom: the spectral decomposition of the variable near-IR spectrum (black) into an accretion disk spectrum (dotted black line) and a hot dust component (red spectrum) yields a blackbody temperature of $T \sim 1200 \text{ K}$ for the latter (dotted red curve).

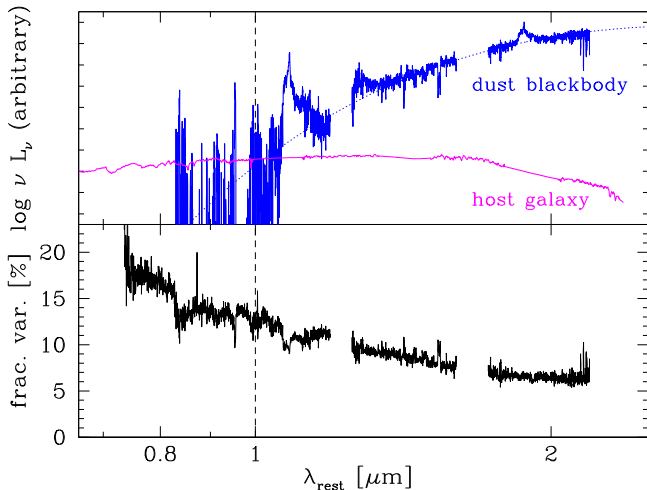


Figure 5. Top: the flux difference between the normalized mean and variable spectra (blue) can be attributed to an additional (constant) dust component with a blackbody temperature of $T \sim 1300 \text{ K}$ (dotted blue line). The template of an elliptical host galaxy is also shown (magenta). Bottom: the fractional amplitude of the variations as a percentage of the mean flux vs. rest-frame wavelength.

$T \sim 1300 \text{ K}$, in Figure 5 (top panel). Since the host galaxy of Mrk 876 is unusually luminous (e.g., Bentz et al. 2009), we have also considered the possibility that some of the spectral difference between the mean and rms spectrum is induced by this constant component. In Figure 5 (top panel), we have included the template of an elliptical galaxy. It is clear that a significant contribution from this component is unlikely, given that the flux difference between the mean spectrum and rms

spectrum increases with wavelength, whereas the host galaxy spectral flux shows the opposite behavior.

Therefore, the hot dust seems to be composed of at least two components with very different variability timescales or behaviors. The secondary dust component present in the mean spectrum appears constant in our campaign, either because it is truly constant or because it varies on timescales that are not probed by our monitoring campaign. If such a constant dust component is indeed present, then the variable dust component does not seem to dominate the total dust emission and constitutes only $\sim 30\%$ of it. A spectral decomposition of the variable near-IR spectrum, conducted as in Section 4, yields its blackbody temperature as $T \sim 1200 \text{ K}$ (Figure 4, bottom panel), which is slightly lower than the average value of the total dust emission of $\langle T \rangle \sim 1300 \text{ K}$.

As an alternative explanation for the observed rms near-IR spectrum in Figure 4, it is conceivable that the deficit in fractional variability at wavelengths $\gtrsim 1.2 \mu\text{m}$ is not due to the presence of a secondary constant dust component, but rather introduced by the anticorrelation of the variability of the near-IR accretion disk flux and the hot dust flux, with the latter varying in delayed response to the former. In such a case, we expect the total variability signal in the near-IR to be a superposition of the two variability signals, so the spectral shape of the rms spectrum should depend on the interplay between them. This superposition can then either enhance or weaken the total variance relative to the mean. In the following, we have simulated this situation with the Differential Evolution Markov Chain (DEMC) formalism, assuming that the secondary variable near-IR component is the accretion disk itself.

The DEMC algorithm was developed by Schnülle et al. (2015) to suit multiband optical/near-IR photometric dust reverberation campaigns, and it can effectively construct the rms spectrum over this entire wavelength range. The analysis is carried out in two steps. First, the structure function parameters for the accretion disk variability are derived from modeling the optical light curve with maximum likelihood, based on the method for the interpolation and reconstruction of noisy irregularly sampled data by Rybicki & Press (1992). The covariance function of the underlying Gaussian Process model is assumed to be a power law (e.g., Press et al. 1992; Schmidt et al. 2010; Hernitschek et al. 2015), and the corresponding structure function can be written as:

$$V(|t - t'|) = A^2 \left(\frac{t - t'}{1 \text{ yr}} \right)^\gamma, \quad (2)$$

where A is the amplitude of the variability on a 1 yr timescale and γ is the gradient of this variability. Second, a model consisting of the sum of a power law, which represents the accretion disk emission, and a single blackbody, which represents the hot dust emission, is fit to the simultaneous multiband optical/near-IR data. This model is:

$$f_\lambda(\lambda, t, \mathbf{x}) = C_1 f_g(t) \lambda^{-\alpha} + C_2 \frac{2hc^2}{\lambda^5} \frac{1}{e^{(hc/\lambda k_B T(t))} - 1}, \quad (3)$$

where $f_g(t)$ and α are the variable accretion disk flux in the optical and the spectral power-law index, respectively, h is the Planck constant, and k_B is the Boltzmann constant. The dust model temperature $T(t)$ evolves with time from an initial value T_0 , as $dT(t)/T(t) = \nu \cdot 0.25 df_g(t - \tau)/f_g(t - \tau)$, in response to the variable accretion disk flux $f_g(t - \tau)$. The accretion disk flux is time-shifted by τ and processed with an efficiency ν (with $0 < \nu < 1$). The posterior distribution of the vector, consisting of six parameters $\mathbf{x} = (C_1, C_2, \nu, \alpha, T_0, \tau)$, is sampled by the DEMC (Ter Braak 2006) algorithm, which is basically a Markov Chain Monte Carlo algorithm, with multiple chains run in parallel. The algorithm evaluates the posterior probability density function for each iteration step and for each chain, given uniform priors within sensible limits.

For the simulations, we assume a fixed campaign length of 1000 days and model the input light curve with stochastic short-term variability overlaid with a roughly sinusoidal long-term variability, with a period length of ~ 400 days. As the light curves presented in Miller et al. (2023) show, this is a reasonable assumption for the variability pattern of the accretion disk in Mrk 876, which exhibits a quasi-oscillatory trend over a time period of about 3 yr. Their data cover two peaks and two troughs of the long-term variability pattern, roughly indicating a period length of about twice the dust response time. We then choose response times of the hot dust emission relative to the variable (optical) accretion disk fluxes of $\tau = 50, 100, 150,$ and 200 lt-days. In addition, we vary the processing efficiency of the dust and assume values of $\nu = 0.5, 0.8,$ and 1 , with the latter producing the maximum possible dust flux variability. Figure 6 shows our results. It is clear that this model of two variable near-IR components can qualitatively reproduce the observations. The strongest depression of the hot dust variations is achieved for a combination of the response time that gives the maximal weakening of the total near-IR variability signal—i.e., half the period length, so ~ 200 lt-days

—and an intrinsically reduced fractional variability of the hot dust emission due to a low processing efficiency. As the accretion disk flux contribution to the total near-IR flux decreases with wavelength (see Figure 3), so does its weakening effect on the dust variability signal, and the dust blackbody can always dominate the rms spectrum at the longest wavelengths. If a secondary variable near-IR component is indeed present at $\sim 2 \mu\text{m}$ and it is the accretion disk, then the implied outer radius is $r_{\text{out}} \sim 4300 r_g \sim 56$ lt-days. Such an accretion disk is likely to harbor dust, which can contribute to the total blackbody emission. We will argue this case further in Section 6.3. Finally, we note that a reduced value of ν in our simulations has a similar effect as adding a constant dust component, i.e., it decreases the dust fractional variability. Therefore, it is conceivable that the observed rms spectrum of Mrk 876 is a combination of both the scenarios described above.

6. The Dust Structure in Mrk 876

It is of great interest to understand the chemical composition and grain size distribution of the circumnuclear dust in AGNs, which can ultimately reveal how cosmic dust forms and evolves in different environments. If we can also constrain where the dust forms, we can assess its relationship to and influence on the other central structures of AGNs, such as, e.g., the BLR and accretion disk. As Landt et al. (2019) have shown, a spectroscopic near-IR reverberation mapping campaign that uses cross-dispersed data covering a very wide wavelength range is ideally suited to investigating these questions. In the following, we discuss our results for Mrk 876, with focuses on: how the combination of a luminosity-based dust radius with a contemporaneous dust response time can constrain the astrochemistry of the dust (Section 6.1); how the simultaneous measurement of the dust temperature and the dust radius can shed light on the dust's geometrical structure (Section 6.2); and the potential of a near-IR variable (rms) spectrum to unravel the structures of accretion disks in AGNs (Section 6.3). Finally, we relate our results to AGN studies at other wavelengths, and develop a new paradigm that connects AGNs and protoplanetary disks (Section 6.4).

6.1. The Astrochemistry of the Hot Dust

From the radiative equilibrium relationship (Equation (1)) it is clear that if estimates of the dust temperature T and irradiating luminosity L_{UV} are available, and if the dust radius can be measured by an independent method, the dust emissivity parameter Q^{em} , which strongly depends on the dust chemical species and grain size, can be constrained. Independent measures of the dust radius can come from, e.g., the dust response time measured through reverberation mapping, a geometric measurement based on near-IR interferometry, or a polarimetric estimate of the location of the scattering region.

Our near-IR spectroscopic data do not extend over a time period that is long enough to be able to derive a reliable dust response time for Mrk 876. However, the WISE monitoring data for the years 2010–2018 analyzed by Lyu et al. (2019) overlap with our campaign, and the W1 band ($3.4 \mu\text{m}$) is expected to sample the same hot dust component by covering its flux close to the SED maximum (see Figure 3). Lyu et al. (2019) estimated a dust response time of $\tau = 297 \pm 17$ lt-days (observer frame) for the W1 band, assuming no corrections (see

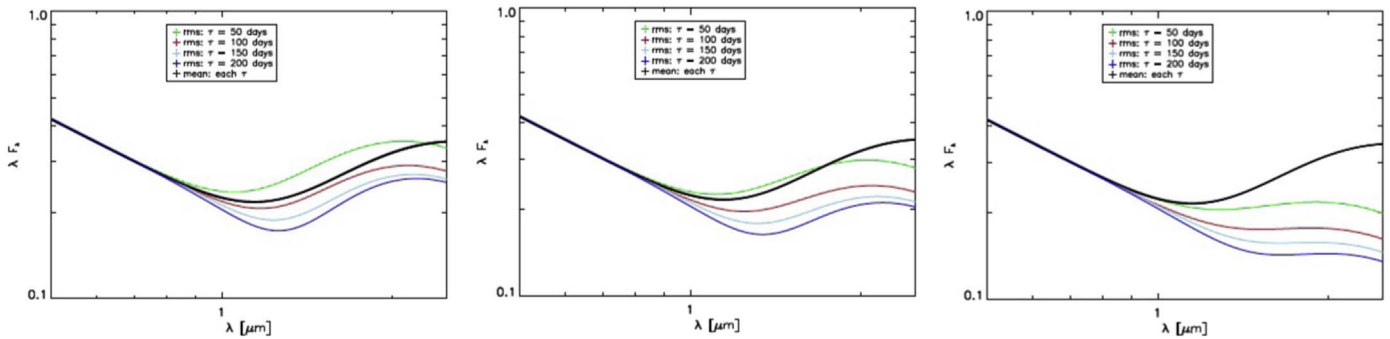


Figure 6. Simulations of the mean (black line) and rms spectra (colored lines) with the DEMC formalism, assuming a secondary variable component at near-IR wavelengths, which is produced by the accretion disk emission. The rms spectra are simulated for four different dust response times ($\tau = 50, 100, 150,$ and 200 lt-days, indicated by the solid green, red, light blue, and dark blue lines, respectively) and three different values of the dust processing efficiency ($\nu = 1, 0.8,$ and 0.5 , shown in the left, middle, and right panels, respectively).

their Figure 5). Adjusting the initial guesses for their fitting routine, based on cross-correlation function results, the revised value was $\tau = 372 \pm 63$ lt-days (see their Table 4). Their result is consistent with the distance to the equatorial scattering region of 254 ± 39 lt-days (rest frame) estimated by Afanasiev et al. (2019), based on spectropolarimetric observations from 2015. Furthermore, the dust response time in Mrk 876 appears to remain relatively constant. From an optical/near-IR photometry campaign during the years 2003–2007, Minezaki et al. (2019) obtained values similar to Lyu et al. (2019) of $\tau = 320 \pm 34, 327^{+42}_{-36},$ and 327^{+41}_{-35} lt-days (observer frame), assuming three different power-law spectral slopes for the accretion disk spectrum when decomposing the flux in the K band.

This independent measure of the dust radius of ~ 300 lt-days is smaller than all the average dust radii that we estimated from thermal equilibrium considerations. The least discrepancy is found relative to the case of a pure blackbody ($\langle R_{\text{d,lum}} \rangle = 469 \pm 30$ lt-days), which corresponds to dust composed of large grains. The average luminosity-based radius for dust of small grains is much larger and exceeds the dust response time by factors $\gtrsim 10$ and $\gtrsim 16$ for carbon and silicate dust, respectively. Therefore, it seems that the hot dust in Mrk 876 is dominated by grains with sizes of at least a few microns, as found for NGC 5548 by Landt et al. (2019). However, contrary to the case of NGC 5548, the luminosity irradiating the dust in Mrk 876 appears to be only a fraction of the bolometric luminosity that we see. Alternatively, if the dust is exposed to the total bolometric luminosity, something must reduce its temperature. In this case, it is worth noting that the response-weighted dust radius predicts a dust temperature of $T \sim 1700$ K, which is close to the sublimation temperature for carbonaceous dust ($T_{\text{sub}} \sim 1800\text{--}2000$ K; Salpeter 1977). Carbonaceous dust was found to be the dominant species in the hot dust of NGC 5548.

It was previously postulated that the circumnuclear dust in AGNs is dominated by large grains (e.g., Laor & Draine 1993; Maiolino et al. 2001). The spectroscopic near-IR monitoring campaigns on NGC 5548 and Mrk 876 have shown that this is indeed the case. Furthermore, they put an important lower limit on the dust grain size of a few microns, which suggests that the hot dust is assembled in a disk-like structure. When the dust grains are very small, their coupling to the ambient gas is strong and Brownian motion dominates the collision rate. Brownian motion-driven agglomeration can efficiently grow micron-sized dust particles, but the induced collision velocity decreases with increasing aggregate mass. Then, as the dust

grains grow, they increasingly decouple from the gas and differential settling becomes the main driver for grain collisions and thus further grain growth (Weidenschilling 1977; Blum & Wurm 2008). Therefore, large dust grains are mainly expected to be found in the midplane of a disk-like structure. If the gas is turbulent, we expect it to drive the diffusion of the dust in the vertical direction, which will oppose the effect of vertical settling and give the disk-like dust structure a scale height.

6.2. The Enlarged Dust-free Inner Hole

The lower dust response time in Mrk 876 relative to the dust radius estimated from radiative equilibrium considerations contrasts with the findings of Landt et al. (2019) for NGC 5548, where the two dust radii were similar. However, it is in line with general comparisons between interferometric dust radii and those determined by photometric reverberation campaigns; the former have been found to be larger than the latter by a factor of ~ 2 (Kishimoto et al. 2009, 2011; Koshida et al. 2014). Since interferometry effectively measures the luminosity-weighted radius, this result can be understood if one assumes that response-weighted radii are dominated by dust that is located at the smallest radii, whereas luminosity-weighted radii are dominated by dust grains with the highest emissivity, i.e., the hottest and largest grains. Due to their lower heat capacity, the highest temperature that large grains can attain will always be lower than the highest temperature that small grains can be heated to, so their emission will come from farther out. We can easily rule out this scenario for Mrk 876, since the blackbody temperatures in the mean and rms near-IR spectra are similar.

Alternatively, Kawaguchi & Mori (2010, 2011) have ascribed the observed difference between response- and luminosity-weighted dust radii to a concave (or bowl-shaped) dust geometry. Due to the anisotropy of the accretion disk emission, dust that is located at larger viewing angles relative to the irradiating UV/optical flux will be reduced by a factor of $\cos \theta$, with θ being the angle between the accretion disk rotation axis and the location of the dust. The interferometric radii would then be dominated by the region containing the bulk of the dust mass, which in this geometry is located farther out, whereas reverberation would simply sample the smallest and thus most variable radii. In this scenario, the concave shape of the dust structure is caused by the assumption of a constant maximum dust temperature, taken to be the dust sublimation temperature, which is found farther away, the higher the

accretion disk luminosity appears to the dust. Our observations for Mrk 876 can be well explained by this scenario. The variable and mean near-IR spectra yield similar dust temperatures, albeit below the sublimation temperature. In order to make the luminosity-based dust radius consistent with the dust response time, we then require that the variable dust sees the bolometric luminosity reduced by a factor of ~ 4 . If our viewing angle to the accretion disk is $\theta = 0^\circ$, as assumed in our calculations of the accretion disk spectrum (Section 4), a variable dust component in a structure inclined at $\theta \sim 75^\circ$, and thus closely aligned with the plane of the accretion disk, would fulfill this requirement. The large dust deficit observed in the rms spectrum relative to the mean spectrum (Section 5) would then be due to the fact that the total emission is dominated by the much larger dust mass located farther out, which appears constant, since it varies on much longer timescales than our campaign is sensitive to.

An indication that the accretion disk illumination anisotropy considered by Kawaguchi & Mori (2010, 2011) differently affects low- and high-luminosity AGNs was also found by Minezaki et al. (2019). Their sample, which included NGC 5548 and Mrk 876 at the low- and high-luminosity ends, respectively, and spanned about four orders of magnitude in luminosity, showed a best-fit slope for the logarithmic reverberation dust radius versus optical luminosity relationship of ~ 0.4 , i.e., shallower than the slope of 0.5 predicted by thermal equilibrium considerations. Interestingly, using the dust response time and average accretion disk luminosity for NGC 5548 as determined by Landt et al. (2019), and the values of these parameters for Mrk 876 from our study, we also derive a slope of ~ 0.4 . Clearly, it would be worthwhile to further populate the undersampled top end of the relationship between the dust radius and the optical continuum luminosity in order to investigate how the dust irradiation pattern depends on the accretion disk luminosity.

But one of our most important results cannot be explained solely with the scenario of Kawaguchi & Mori (2010, 2011), although the implied flared disk-like structure for the hot dust helps. Similar to what Landt et al. (2019) observed in NGC 5548, the hot dust in Mrk 876 is not close to its sublimation temperature. This finding implies the presence of an enlarged dust-free inner region in AGNs and thus a luminosity-invariant inner edge of the torus, i.e., a “torus wall.” Since the sublimation temperature for carbon dust is higher than that for silicate dust (~ 1900 K and ~ 1400 K, respectively), the extent of this “inner hole” would be considerably larger if the former chemical species indeed dominates the dust composition. Such a dusty wall has been confirmed for NGC 4151 with several epochs of both interferometric and reverberation dust radius measurements (Koshida et al. 2009; Pott et al. 2010; Schnülle et al. 2013). This paradigm for the AGN dust structure is similar to the standard picture of protoplanetary disks around young stars. In many of these disks, interferometry finds that the inner dust radius is significantly larger than the dust sublimation radius. This cavity, which is commonly referred to as the “inner hole,” is believed to be filled with gaseous disk material that can change its optical thickness and thus influence the location of the puffed-up “wall” or “inner rim” of the dusty, flared, and passively illuminated protoplanetary disk (Monnier et al. 2005; Dullemond & Monnier 2010). Our result, that circumnuclear AGN dust is composed of relatively large grains, has also been

found for protoplanetary disks (van Boekel et al. 2004; Kóspál et al. 2020). We will explore in more detail the similarity between these two classes of astrophysical objects in Section 6.4.

6.3. A Secondary Hot Dust Component

In Section 5, we showed that the observation of a reduced dust emission in the rms near-IR spectrum of Mrk 876 relative to its mean spectrum can also be explained by the accretion disk spectrum extending well into the near-IR. The implied large disk radii were ~ 25 and ~ 56 lt-days in the *J* and *K* bands, respectively. These values are similar to estimates from a contemporaneous accretion disk reverberation mapping campaign. Miller et al. (2023) recently presented an accretion disk analysis using optical photometric monitoring in several bands (*u*, *g*, *r*, *i*, and *z*) conducted between 2016 March and 2019 May, including our data set as presented in Section 3.2. They found that the response times depended on the wavelength, as expected for a standard thin disk. Then, by extrapolating their optical response times to the near-IR, they estimated outer disk radii of ~ 20 and ~ 45 lt-days in the *J* and *K* bands, respectively. Given these extents, it is of interest to understand whether they are large enough to potentially harbor dust.

We can estimate the location of the accretion disk dust, if it exists, as follows. First, we use the simultaneous measurements of the dust temperature in the rms spectrum and the dust response time for the variable hot dust component, together with the emissivity law that we determine in Section 6.1, to “calibrate” the temperature–radius relationship for the dust and thus to estimate the bolometric luminosity that produces it. We show this relationship, which is that of a blackbody, and thus has the form $T \propto R^{-0.5}$, in Figure 7 (solid red line). As we have already discussed in Section 6.2, the corresponding total bolometric luminosity that seems to irradiate the dust is $\log L_{\text{bol}} \sim 45.5$ erg s $^{-1}$, which is a factor of ~ 4 lower than the average bolometric luminosity of $\log L_{\text{uv}} = 46.09 \pm 0.03$ erg s $^{-1}$, estimated from fits to the near-IR spectra. Assuming that this irradiating luminosity is produced by an accretion disk, we then calculate the temperature–radius relationship for it, which is of the standard form $T \propto R^{-0.75}$, and so steeper than that for the hot dust (solid black line). These curves immediately show that dust is expected to condense out in the accretion disk gas at much smaller radii than those possible for gas exposed to the full bolometric luminosity. Then, if this dust were to be driven off the accretion disk, e.g., by a dusty outflow, it would quickly be destroyed at considerable heights (Czerny et al. 2017). For the observed dust temperature, we expect the accretion disk of Mrk 876 to become dusty at radii $\gtrsim 40$ lt-days. This secondary hot dust will not necessarily be externally illuminated and so reverberate in the classical sense. Instead, if it is composed of micron-sized grains, it will be well coupled to the gas and vary on the same timescales. Dust with a variability on such short timescales is likely to appear constant in our rms near-IR spectrum.

An additional argument for the reality of a secondary hot dust component in Mrk 876 can also be derived from the total observed dust luminosity. The values listed in Table 2 (column (4)) give an average of $\log L_{\text{d}} = 45.55 \pm 0.02$ erg s $^{-1}$, which, if interpreted as being produced by a single dust component (e.g., with the geometry proposed by Kawaguchi & Mori 2010), implies a dust covering factor of unity, given the “calibrated” bolometric luminosity irradiating it. Given that the hot dust is

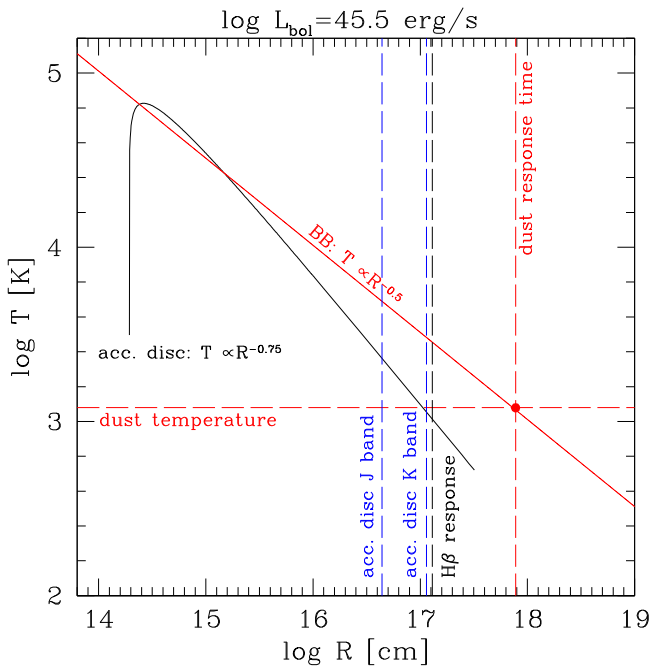


Figure 7. The temperature–radius relationships for the hot dust (red curve) and the accretion disk illuminating it (black curve). They correspond to a bolometric luminosity of $\log L_{\text{bol}} = 45.5 \text{ erg s}^{-1}$, which we derive from “calibrating” the relationship for the hot dust to its observed temperature in the rms near-IR spectrum and the rest-frame dust response time ($T = 1200 \text{ K}$ and $R_{\text{d,rev}} = 300 \text{ lt-days}$; shown as the horizontal and vertical red dashed lines, respectively). The blue dashed lines indicate the accretion disk reverberation radii of ~ 20 and $\sim 45 \text{ lt-days}$ estimated by Miller et al. (2023) for the *J* and *K* bands, respectively. The vertical black dashed line indicates the $\text{H}\beta$ BLR response time of $\sim 50 \text{ lt-days}$ measured by Bao et al. (2022).

optically thick to the UV/optical accretion disk luminosity, such an AGN would be an obscured Compton-thick one. On the other hand, if we assume an additional dust component in the mean spectrum, the rms spectrum tells us that the variable dust component makes up roughly only a third of the total observed dust flux, and so has a covering factor of $\sim 30\%$. We note that, by coincidence, we would also estimate a similar value for the covering factor from the mean spectrum alone, since both the bolometric luminosity illuminating the torus dust and the dust luminosity would be overestimated by a similar factor. If the dust deficit in the rms spectrum were to appear exacerbated, due to the influence of the variable accretion disk (and possibly its associated dust), as discussed in Section 5, then the torus dust covering factor would be higher.

The first tentative evidence for dust in the accretion disk was found by Landt et al. (2019), for NGC 5548. If it can be shown that such dust is ubiquitous in AGNs, it would provide a possible connection to the BLR in models of radiatively accelerated dusty outflows that are launched from the outer accretion disk (e.g., Elitzur & Shlosman 2006; Czerny et al. 2016, 2017; Esser et al. 2019). In this case, carbon dust would provide the largest opacity and lead to an inflated disk structure (Baskin & Laor 2018). Support for this scenario in Mrk 876 comes from the remarkable agreement between the location that we estimated for the accretion disk dust and the $\text{H}\beta$ BLR radius of $\sim 50 \text{ lt-days}$ measured by Bao et al. (2022), for their reverberation mapping campaign conducted between 2016 December and 2018 May. Disk-like dust structures in AGNs have also started to be revealed by interferometric observations

achieving an unprecedented high spatial resolution in the mid-IR (Isbell et al. 2022).

6.4. Are AGNs and Protoplanetary Disks Similar?

Large accretion disks that extend well beyond the self-gravity radius are now routinely inferred for AGNs by accretion disk reverberation studies (see the review by Cackett et al. 2021). Evidence for the presence of dust in these disks would imply even greater radii, thus exacerbating the stability issue. A possible solution to, and an alternative explanation for, our finding of a significantly reduced bolometric luminosity of the accretion disk in Mrk 876, as seen by the dust, is that it is a passive disk. A passively illuminated disk, such as a protoplanetary disk, has a temperature–radius relationship that is indistinguishable from that of a standard accretion disk that produces its own radiation via gravitational energy release, i.e., it is of the same form $T \propto R^{-0.75}$ (e.g., Cackett et al. 2007). Accretion disk flux variability in AGNs is readily interpreted as reprocessed emission from a central, highly variable, hard X-ray source, since the observed timescales are much shorter than the viscous timescale, i.e., the time that it takes for a change in the accretion rate to trigger a change in the disk temperature and thus the flux. The passively irradiated flux is usually assumed to be only a small fraction of $\sim 10\%$ – 20% of the total disk emission (Starkey et al. 2016; Gardner & Done 2017). The value of $\sim 25\%$ that we estimate for Mrk 876 is close to this range. An advantage of the passive disk scenario over the $\cos \theta$ effect in a bowl-like geometry, such as the one proposed by Kawaguchi & Mori (2010), is that it predicts the onset of dust in the accretion disk around the $\text{H}\beta$ BLR radius; if only an anisotropic accretion disk emission as seen by the dust is assumed, the accretion disk itself would have the total (unreduced) bolometric luminosity and so be hotter, leading to the onset of dust much farther out. We also note that the relative scaling that we obtained between the mean and rms near-IR spectra in the optical regime of a factor of ~ 7 (Section 5) is similar to the factor of ~ 4 reduction in total bolometric luminosity required by the variable dust. Therefore, it could well be that the dust is irradiated only by the variable reprocessed disk flux.

Passive disks can be distinguished from standard accretion disks, since, as a consequence of vertical hydrostatic equilibrium, they are flared, with the disk relatively thicker at larger radii. The vertically isothermal flared disk diverges from the flat disk solution at intermediate radii and approaches $T \propto R^{-3/7}$ at large radii, i.e., it is very similar to a single blackbody (e.g., Kenyon & Hartmann 1987). The dust is crucial for the disk thermodynamics (and for planet formation), but it represents only $\sim 1\%$ of the total mass and is easier to observe than the gas. Self-gravity is generally only significant in very massive disks, and protoplanetary disks are often not massive enough to become gravitationally unstable. It is then conceivable that in Mrk 876, the sum of both the temperature–radius profiles displayed in Figure 7 (the solid black and red lines) represents a single entity, namely a passively illuminated flared dusty disk. A wind off this disk could then be the origin of the BLR.

7. Summary and Conclusions

We have conducted the first spectroscopic near-IR monitoring campaign on Mrk 876, one of the intrinsically most

luminous AGNs in the nearby universe. Our cross-dispersed spectroscopy can measure dust temperatures with high precision, allowing us to derive the luminosity-based dust radii for different grain properties. When comparing these to an independent measure of the dust radius, we can then constrain the astrochemistry of the hot dust. Furthermore, we can construct the variable (rms) near-IR spectrum over a relatively large wavelength range.

Our main results can be summarized as follows.

(i) Assuming thermal equilibrium for optically thin dust, we find that the luminosity-based dust radii are larger than the dust response time obtained by a contemporaneous photometric reverberation mapping campaign, with the least discrepancy (of a factor of ~ 2) found relative to the result for a wavelength-independent dust emissivity law, i.e., a blackbody, which is appropriate for grains of relatively large sizes (of a few microns). This result can be well explained by a flared disk-like structure for the hot dust, whereby the anisotropy of the accretion disk emission causes a decrease in illumination (by a factor of ~ 4 , in our case), as first proposed by Kawaguchi & Mori (2010, 2011).










(ii) The near-IR variable (rms) spectrum tracks the accretion disk spectrum out to longer wavelengths (of $\sim 1.2 \mu\text{m}$) than the mean spectrum (of $\sim 1 \mu\text{m}$), due to the reduced dust emission in the former. The implied outer accretion disk radius is much larger than the self-gravity radius, and consistent with the extrapolated results from the contemporaneous multiband optical accretion disk reverberation mapping campaign of Miller et al. (2023). The flux variability of the hot dust with respect to the accretion disk is reduced by a factor of ~ 3 , and this could be due to either the presence of a secondary hot dust component in the mean spectrum or the destructive superposition of the dust and accretion disk variability signals, or some combination of the two.

(iii) The large extent of the accretion disk, which is likely to harbor dust in its outer regions, and the low bolometric luminosity, as seen by the hot dust, can also be explained if we assume that AGN disks are similar to protoplanetary disks around young stars. A passively illuminated flared dusty disk would naturally provide a single continuous structure for the temperature–radius profile determined by AGN accretion disk reverberation studies ($T \propto R^{-3/4}$) at small radii, and for that of the hot dust blackbody ($T \propto R^{-1/2}$), determined here at large radii.

H.L. is indebted to Brad Peterson for suggesting the science target and leading the IR observing proposals and to Peter Abrahám, Ágnes Kóspál, and Hubert Klahr for generously sharing their knowledge about protoplanetary disks. H.L. and J.A.J.M. thank Michael Fausnaugh for help with applying his MAPSPEC routine to the near-IR spectroscopy. H.L. acknowledges a Daphne Jackson Fellowship, sponsored by the Science and Technology Facilities Council (STFC), UK. J.A.J.M. acknowledges the support of STFC studentship ST/S50536/1. H.L., J.A.J.M., and M.J.W. acknowledge support from STFC grants ST/P000541/1 and ST/T000244/1. K.H. and J.V.H.S. acknowledge support from STFC grant ST/R000824/1. E.R. C. acknowledges the support of the South African National Research Foundation.

Facilities: Gemini (GNIRS), LCOGT (optical).

ORCID iDs

Hermine Landt  <https://orcid.org/0000-0001-8391-6900>
 Martin J. Ward  <https://orcid.org/0000-0003-1810-0889>
 Jörg-Uwe Pott  <https://orcid.org/0000-0003-4291-2078>
 Keith Horne  <https://orcid.org/0000-0003-1728-0304>
 Juan V. Hernández Santisteban  <https://orcid.org/0000-0002-6733-5556>
 Edward M. Cackett  <https://orcid.org/0000-0002-8294-9281>
 Michael R. Goad  <https://orcid.org/0000-0002-2908-7360>
 Encarni Romero Colmenero  <https://orcid.org/0000-0003-0607-1136>
 Hartmut Winkler  <https://orcid.org/0000-0003-2662-0526>

References

- Afanasyev, V. L., Popović, L. Č., & Shapovalova, A. I. 2019, *MNRAS*, **482**, 4985
- Antonucci, R. 1993, *ARA&A*, **31**, 473
- Bao, D.-W., Brotherton, M. S., Du, P., et al. 2022, *ApJS*, **262**, 14
- Baskin, A., & Laor, A. 2018, *MNRAS*, **474**, 1970
- Bentz, M. C., Denney, K. D., Grier, C. J., et al. 2013, *ApJ*, **767**, 149
- Bentz, M. C., & Katz, S. 2015, *PASP*, **127**, 67
- Bentz, M. C., Peterson, B. M., Netzer, H., Pogge, R. W., & Vestergaard, M. 2009, *ApJ*, **697**, 160
- Blum, J., & Wurm, G. 2008, *ARA&A*, **46**, 21
- Brown, M. J. I., Duncan, K. J., Landt, H., et al. 2019, *MNRAS*, **489**, 3351
- Brown, T. M., Baliber, N., Bianco, F. B., et al. 2013, *PASP*, **125**, 1031
- Buchanan, C. L., Gallimore, J. F., O’Dea, C. P., et al. 2006, *AJ*, **132**, 401
- Burtscher, L., Meisenheimer, K., Tristram, K. R. W., et al. 2013, *A&A*, **558**, A149
- Cackett, E. M., Bentz, M. C., & Kara, E. 2021, *iSci*, **24**, 102557
- Cackett, E. M., Horne, K., & Winkler, H. 2007, *MNRAS*, **380**, 669
- Clavel, J., Wamsteker, W., & Glass, I. S. 1989, *ApJ*, **337**, 236
- Cooke, A., & Rodgers, B. 2005, in ASP Conf. Ser. 347, *Astronomical Data Analysis Software and Systems XIV*, ed. P. Shopbell, M. Britton, & R. Ebert (San Francisco, CA: ASP), 514
- Czerny, B., Du, P., Wang, J.-M., & Karas, V. 2016, *ApJ*, **832**, 15
- Czerny, B., Li, Y.-R., Hryniewicz, K., et al. 2017, *ApJ*, **846**, 154
- Dickey, J. M., & Lockman, F. J. 1990, *ARA&A*, **28**, 215
- Draine, B. T. 2016, *ApJ*, **831**, 109
- Dullemond, C. P., & Monnier, J. D. 2010, *ARA&A*, **48**, 205
- Elias, J. H., Joyce, R. R., Liang, M., et al. 2006, *Proc. SPIE*, **6269**, 62694C
- Elitzur, M., & Shlosman, I. 2006, *ApJL*, **648**, L101
- Esser, J., Pott, J. U., Landt, H., & Vacca, W. D. 2019, *A&A*, **621**, A46
- Fausnaugh, M. M. 2017, *PASP*, **129**, 024007
- Fischer, T. C., Crenshaw, D. M., Kraemer, S. B., et al. 2015, *ApJ*, **799**, 234
- Fischer, T. C., Machuca, C., Diniz, M. R., et al. 2017, *ApJ*, **834**, 30
- Gámez Rosas, V., Isbell, J. W., Jaffe, W., et al. 2022, *Natur*, **602**, 403
- Gardner, E., & Done, C. 2017, *MNRAS*, **470**, 3591
- Glass, I. S. 2004, *MNRAS*, **350**, 1049
- Gravity Collaboration, Dexter, J., Shangquan, J., et al. 2020, *A&A*, **635**, A92
- Grier, C. J., Martini, P., Watson, L. C., et al. 2013, *ApJ*, **773**, 90
- Hao, H., Elvis, M., Civano, F., et al. 2010, *ApJL*, **724**, L59
- Hernández Santisteban, J. V., Edelson, R., Horne, K., et al. 2020, *MNRAS*, **498**, 5399
- Hermitschek, N., Rix, H.-W., Bovy, J., & Morganson, E. 2015, *ApJ*, **801**, 45
- Hönig, S. F., Kishimoto, M., Tristram, K. R. W., et al. 2013, *ApJ*, **771**, 87
- Horne, K., De Rosa, G., Peterson, B. M., et al. 2021, *ApJ*, **907**, 76
- Isbell, J. W., Burtscher, L., Asmus, D., et al. 2021, *ApJ*, **910**, 104
- Isbell, J. W., Meisenheimer, K., Pott, J. U., et al. 2022, *A&A*, **663**, A35
- Kawaguchi, T., & Mori, M. 2010, *ApJL*, **724**, L183
- Kawaguchi, T., & Mori, M. 2011, *ApJ*, **737**, 105
- Kenyon, S. J., & Hartmann, L. 1987, *ApJ*, **323**, 714
- Kirkpatrick, A., Pope, A., Sajina, A., et al. 2015, *ApJ*, **814**, 9
- Kishimoto, M., Antonucci, R., Blaes, O., et al. 2008, *Natur*, **454**, 492
- Kishimoto, M., Hönig, S. F., Antonucci, R., et al. 2009, *A&A*, **507**, L57
- Kishimoto, M., Hönig, S. F., Antonucci, R., et al. 2011, *A&A*, **527**, A121
- Kishimoto, M., Hönig, S. F., Beckert, T., & Weigelt, G. 2007, *A&A*, **476**, 713
- Koratkar, A., & Blaes, O. 1999, *PASP*, **111**, 1
- Koshida, S., Minezaki, T., Yoshii, Y., et al. 2014, *ApJ*, **788**, 159
- Koshida, S., Yoshii, Y., Kobayashi, Y., et al. 2009, *ApJL*, **700**, L109
- Kóspál, Á., Abrahám, P., Carmona, A., et al. 2020, *ApJL*, **895**, L48
- Landt, H., Bentz, M. C., Peterson, B. M., et al. 2011a, *MNRAS*, **413**, L106

- Landt, H., Bentz, M. C., Ward, M. J., et al. 2008, *ApJS*, **174**, 282
- Landt, H., Buchanan, C. L., & Barmby, P. 2010, *MNRAS*, **408**, 1982
- Landt, H., Elvis, M., Ward, M. J., et al. 2011b, *MNRAS*, **414**, 218
- Landt, H., Ward, M. J., Elvis, M., & Karovska, M. 2014, *MNRAS*, **439**, 1051
- Landt, H., Ward, M. J., Kynoch, D., et al. 2019, *MNRAS*, **489**, 1572
- Laor, A., & Draine, B. T. 1993, *ApJ*, **402**, 441
- Lawrence, A. 1987, *PASP*, **99**, 309
- Lobban, A., & King, A. 2022, *MNRAS*, **511**, 1992
- Lyu, J., & Rieke, G. 2022a, *Univ*, **8**, 304
- Lyu, J., & Rieke, G. H. 2018, *ApJ*, **866**, 92
- Lyu, J., & Rieke, G. H. 2022b, *ApJ*, **940**, L31
- Lyu, J., Rieke, G. H., & Smith, P. S. 2019, *ApJ*, **886**, 33
- Maiolino, R., Marconi, A., & Oliva, E. 2001, *A&A*, **365**, 37
- McCully, C., Volgenau, N. H., Harbeck, D.-R., et al. 2018, *Proc. SPIE*, **10707**, 107070K
- Miller, J. A., Cackett, E. M., Goad, M. R., et al. 2023, *ApJ*, in press
- Minezaki, T., Yoshii, Y., Kobayashi, Y., et al. 2019, *ApJ*, **886**, 150
- Monnier, J. D., Millan-Gabet, R., Billmeier, R., et al. 2005, *ApJ*, **624**, 832
- Nelson, B. O. 1996, *ApJL*, **465**, L87
- Nenkova, M., Sirocky, M. M., Ivezić, Z., & Elitzur, M. 2008, *ApJ*, **685**, 147
- Netzer, H. 2015, *ARA&A*, **53**, 365
- Oknyanskij, V. L., & Horne, K. 2001, in ASP Conf. Ser. 224, Probing the Physics of Active Galactic Nuclei, ed. B. M. Peterson, R. W. Pogge, & R. S. Polidan (San Francisco, CA: ASP), 149
- Peterson, B. M., Ferrarese, L., Gilbert, K. M., et al. 2004, *ApJ*, **613**, 682
- Phinney, E. S. 1989, in NATO Advanced Study Institute (ASI) Series C, Vol. 290, Theory of Accretion Disks, ed. F. Meyer (Dordrecht: Kluwer Academic), 457
- Pott, J.-U., Malkan, M. A., Elitzur, M., et al. 2010, *ApJ*, **715**, 736
- Press, W. H., Rybicki, G. B., & Hewitt, J. N. 1992, *ApJ*, **385**, 404
- Ramos Almeida, C., Levenson, N. A., Alonso-Herrero, A., et al. 2011, *ApJ*, **731**, 92
- Rybicki, G. B., & Press, W. H. 1992, *ApJ*, **398**, 169
- Salpeter, E. E. 1977, *ARA&A*, **15**, 267
- Schmidt, K. B., Marshall, P. J., Rix, H.-W., et al. 2010, *ApJ*, **714**, 1194
- Schnülle, K., Pott, J.-U., Rix, H.-W., et al. 2013, *A&A*, **557**, L13
- Schnülle, K., Pott, J.-U., Rix, H.-W., et al. 2015, *A&A*, **578**, A57
- Skrutskie, M. F., Cutri, R. M., Stiening, R., et al. 2006, *AJ*, **131**, 1163
- Soubiran, C., Le Campion, J.-F., Brouillet, N., & Chemin, L. 2016, *A&A*, **591**, A118
- Starkey, D. A., Horne, K., & Villforth, C. 2016, *MNRAS*, **456**, 1960
- Storchi-Bergmann, T., McGregor, P. J., Riffel, R. A., et al. 2009, *MNRAS*, **394**, 1148
- Suganuma, M., Yoshii, Y., Kobayashi, Y., et al. 2006, *ApJ*, **639**, 46
- Ter Braak, C. J. F. 2006, *S&C*, **16**, 239
- Tristram, K. R. W., Burtscher, L., Jaffe, W., et al. 2014, *A&A*, **563**, A82
- Tristram, K. R. W., Raban, D., Meisenheimer, K., et al. 2009, *A&A*, **502**, 67
- van Boekel, R., Min, M., Leinert, C., et al. 2004, *Natur*, **432**, 479
- Vazquez, B., Galianni, P., Richmond, M., et al. 2015, *ApJ*, **801**, 127
- Weedman, D. W., Hao, L., Higdon, S. J. U., et al. 2005, *ApJ*, **633**, 706
- Weidenschilling, S. J. 1977, *MNRAS*, **180**, 57